



January 2019

Chromium Selenide Synthesis And Characterization

Alexander Kukay

Follow this and additional works at: <https://commons.und.edu/theses>

Recommended Citation

Kukay, Alexander, "Chromium Selenide Synthesis And Characterization" (2019). *Theses and Dissertations*. 2467.
<https://commons.und.edu/theses/2467>

This Thesis is brought to you for free and open access by the Theses, Dissertations, and Senior Projects at UND Scholarly Commons. It has been accepted for inclusion in Theses and Dissertations by an authorized administrator of UND Scholarly Commons. For more information, please contact zeinebyousif@library.und.edu.

CHROMIUM SELENIDE SYNTHESIS AND CHARACTERIZATION

by

Alexander John Kukay

Bachelor of Science, University of Wisconsin-Eau Claire, 2017

A Thesis

Submitted to the Graduate Faculty

of the

University of North Dakota

in partial fulfillment of the requirements

for the degree of

Master of Science

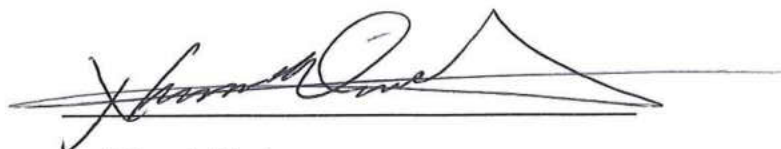
Grand Forks, North Dakota

May


2019

Copyright 2019 Alexander John Kukay

This thesis, submitted by Alexander John Kukay in partial fulfillment of the requirements for the Degree of Master of Science from the University of North Dakota, has been read by the Faculty Advisory Committee under whom the work has been done and is hereby approved.



Nuri Oncel, Chairperson



Kanishka Marasinghe

 04/23/19

Deniz Cakir

This thesis is being submitted by the appointed advisory committee as having met all the requirements of the School of Graduate Studies at the University of North Dakota and is hereby approved.



Dr. Chris Nelson, Associate Dean
School of Graduate Studies



Date

PERMISSION

Title CHROMIUM SELENIDE SYNTHESIS AND CHARACTERIZATION

Department Physics and Astrophysics

Degree Master of Science

In presenting this thesis in partial fulfillment of the requirements for a graduate degree from the University of North Dakota, I agree that the library of this University shall make it freely available for inspection. I further agree that permission for extensively copying for scholar purposes may be granted by the professor who supervised my thesis work or, in his absence, by the Chairperson of the department or the dean of the School of Graduate Studies. It is understood that any copying or publication or other use of this thesis or part thereof for financial gain shall not be allowed without my written permission. It is also understood that due recognition shall be given to me and to the University of North Dakota in any scholarly use which may be made of any material in my thesis.

Alexander John Kukay

April 24, 2019

TABLE OF CONTENTS

LIST OF FIGURES.....	vii
ACKNOWLEDGMENTS.....	x
ABSTRACT.....	xii
CHAPTER	
I. INTRODUCTION.....	1
1.1. Transition Metal Chalcogenides.....	1
1.2. Properties of Cr ₃ Se ₄	2
1.3. Properties of Cr ₂ Se ₃	3
II. EXPERIMENTAL METHODS.....	4
2.1 Reaction Vessels.....	4
2.2 Heat Treatment.....	6
2.3 Deposition on Sapphire.....	7
III. CHARACTERIZATION TECHNIQUES.....	9
3.1 X-ray Diffraction.....	9
3.2 X-ray Photoelectron Spectroscopy	10
3.3 Atomic Force Microscopy.....	15

IV. RESULTS AND DISCUSSION.....	17
4.1 X-ray Diffraction Analysis.....	17
4.2 X-ray Photoelectron Spectroscopy Survey Analysis.....	19
4.3 X-ray Photoelectron Spectroscopy Multiplex Analysis.....	23
4.4 Atomic Force Microscopy Analysis.....	29
V. CONCLUSION.....	36
REFERENCES.....	38

LIST OF FIGURES

Figure 1.1: Periodic table with transition metals (blue) and chalcogens (yellow) highlighted.....	2
Figure 2.1: Schematic of Reaction Vessel 1 with powder sample.....	6
Figure 2.2: Schematic of Reaction Vessel 2 with powder sample.....	6
Figure 2.3: A schematic of depositing synthesized powder on to a sapphire substrate. The particles are carried by argon gas to a landing site placed just outside of the furnace.....	8
Figure 3.1: Schematic of an XPS, an X-ray beam is focused on the sample and ejected electrons are collected by the detector.....	13
Figure 3.2: Schematic of the X-ray source, a filament is heated and excites an aluminum target that in turn generates x-rays that are then focused using electromagnetic lenses and focused on the sample.....	14
Figure 3.3: Schematic of AFM scan head, a cantilever rasters across a sample and as the tip moves up and down, a laser focused on the top of the cantilever changes position. The reflection of the laser is detected via a photodetector and topography data is obtained.....	16

Figure 4.1: XRD results from Sample 1.....	18
Figure 4.2: XRD results from Sample 2.....	19
Figure 4.3: Crystal structures of Cr ₃ Se ₄ and Cr ₂ Se ₃	21
Figure 4.4: XPS survey of Sample 1.....	22
Figure 4.5: XPS survey of Sample 2.....	23
Figure 4.6: Multiplex of Sample 1 Cr 2p peak.....	25
Figure 4.7: Multiplex of Sample 2 Cr 2p peak.....	25
Figure 4.8: Multiplex of Sample 1 Cr 3s peak.....	26
Figure 4.9: Multiplex of Sample 2 Cr 3s peak.....	27
Figure 4.10: Multiplex of Sample 1 Se 3d peak.....	28
Figure 4.11: Multiplex of Sample 2 Se 3d peak.....	28
Figure 4.12: 40 μm x 40 μm topographical image and height profiles of Cr ₃ Se ₄ powder deposited on sapphire substrate.....	31
Figure 4.13: Topographical image and height profiles of Cr ₂ Se ₃ powder deposited on sapphire.....	32
Figure 4.14: 20 μm x 20 μm topographical image and height profile of Cr ₂ Se ₃	

powder deposited on sapphire substrate.....34

Figure 4.15: 5 μm x 5 μm topographical image and height profile of Cr_2Se_3

powder deposited on sapphire substrate.....35

ACKNOWLEDGMENTS

I wish to express my sincere appreciation to the members of my advisory committee for their guidance, support, and genuine interest in my education. The formal meetings as well as open door questions that were too numerous to count have been instrumental in my learning experience.

*To my parents,
for everything*

ABSTRACT

A number of transition metal chalcogenides have displayed promising electrical and magnetic properties that may prove to be ideal materials for various electro-chemical applications. However, production of various transition metal chalcogenides has remains unique to each material and typically these synthesis techniques are not scalable for industrial utilization. Using a generalized heat treatment, various chromium selenium compounds were synthesized. Phase control has been demonstrated by restricting the amount of oxygen present in the reaction vessel. Obtaining different phases as a result of changing an environmental condition suggests a tunable reaction method that can be used to synthesize a number of unique compounds while only changing one parameter. The presence of oxygen drives the composition of chromium to the preferred state, thus effecting the composition of selenium required to create a thermodynamically preferred compound. Since some phases create quasi-two-dimensional materials, a mechanism for controlling phase formation assists in the development and fabrication of devices. Each compound of chromium selenide has a unique crystalline structure, meaning the ability to control the phase formation in effect controls the physical structures itself. Phases of Cr_3Se_4 and Cr_2Se_3 were successfully synthesized and subsequently analyzed with X-ray Diffraction and X-ray Photoelectron Spectroscopy methods. While some phases are antiferromagnetic, other phases have thermoelectric properties. Other phases may prove useful in electrode architecture applications due to the multilayer crystal structure.

CHAPTER I

INTRODUCTION

1.1. Transition Metal Chalcogenides

Transition Metal Chalcogenides (TMCs) are promising class of materials that are comprised of one transition metal, M, and one chalcogen, X, in the form of M_aX_b . These materials can be made out of abundant materials and have a wide range of thermoelectric and electrochemical properties.¹⁻⁶ Because of these exciting properties, these materials have been the focus of a large body of research and continue to be investigated for novel applications. A subset of the materials, Transition Metal Dichalcogenides (TMDs), typically have a two-dimensional layered structure and have brought renewed interest to TMCs as a whole. When present in two dimensional layers, these materials exhibit vastly different electronic and magnetic properties than their bulk crystal counterparts. In the process of investigating monolayer TMDs, many TMCs have been overlooked and may have promising two-dimensional or quasi-two-dimensional structures that likely exhibit different electrochemical or magnetic properties compared to the bulk crystal form.

Two compounds were synthesized and characterized throughout this project, both of which were chromium selenides. Cr_3Se_4 and Cr_2Se_3 powders were synthesized and characterized for potential use in electrochemical or thermoelectric applications. These powders were synthesized by mixing chromium and selenium powders and subjecting the powders to a specific heat treatment procedure. These powders were then characterized to determine the exact composition and crystal structure. After powder characterization, deposited nano-structures from these powders were also characterized.

The image shows a standard periodic table of elements. The transition metals, which are the d-block elements, are highlighted in blue. These include elements from Scandium (Sc) to Zinc (Zn) in the first row, Yttrium (Y) to Cadmium (Cd) in the second, and Lanthanum (La) to Mercury (Hg) in the third. The chalcogens, which are the elements in group 16, are highlighted in yellow. These include Oxygen (O), Sulfur (S), Selenium (Se), and Tellurium (Te). The lanthanide and actinide series are shown at the bottom of the table.

Figure 1.1: Periodic table with transition metals (blue) and chalcogens (yellow) highlighted.

1.2. Properties of Cr_3Se_4

Much interest has been focused around Cr_3Se_4 because it is metallic and shares the same NiAs type structure as Cr_3S_4 when in the bulk formation.⁷⁻¹³ Cr_3Se_4 is a promising thermoelectric due to its small lattice thermal conductivity and high power factor.⁷ Cr_3Se_4 has also been reported to have antiferromagnetic properties with a Neel temperature of 80 K.⁸ Many useful properties of Cr_3Se_4 have been established or reported, showing it a very interesting bulk material that may prove useful to many different disciplines. However, atomically thin Cr_3Se_4 has not been explored and because these properties typically change drastically in the transition from bulk to two-dimensional form, Cr_3Se_4 is an excellent candidate for two-dimensional experimentation and characterization.

1.3. Properties of Cr_2Se_3

Cr_2Se_3 forms the same structure as other NiAs type transition metal chalcogenides and has been shown to exhibit antiferromagnetic properties with a Neel temperature of 43 K in the rhombohedral form along with exhibiting metallic properties.^{3,4,9,12,14-18} Although Cr_2Se_3 is an exciting material in bulk form, it still requires thorough investigation of the two-dimensional form as many electronic properties change dramatically.

CHAPTER II

EXPERIMENTAL METHODS

2.1 Reaction Vessels

Reactions were confined to quartz tube reaction vessels. Two types of vessels were used, one with compressed O-ring seals and a second that was sealed using an oxyacetylene torch. Both tubes were evacuated to a low base pressure, on the order of 10^{-4} Torr. Each reaction chamber design posed unique challenges. The tube with compressed O-ring fittings was easier to load and maintain but the ends of the tube protruded from the furnace, allowing vapor to condense and thus leave the reaction space. This effect also acted as a temperature gradient meaning the internal conditions varied with position and may have had non-quantifiable edge effects. This tube was also found to allow a small amount of air in while the reaction was taking place. Without active vacuum, air entered the reaction vessel and provided excess oxygen resulting in oxidation and unwanted contamination.

The second type of tube employed was more difficult to produce but provided a more controlled environment for the reaction. These vessels were made from a smaller diameter quartz tube and first cut to size with a diamond saw. The exact size of the tube was unimportant as long as it did not protrude from the furnace. The tube was then filled with the reaction materials and sealed under active vacuum with an oxyacetylene torch. This sealing method ensured no excess oxygen was present and kept the sample isolated until analysis. To produce this tube, multiple sealing steps were employed. First the powders were loaded into a tube with one end sealed and then clamped to a stand. The end of the tube was submerged in water to

avoid heating the reaction materials. The use of water as a coolant was an important consideration as the melting point of selenium is 221° C and the temperature of the oxyacetylene flame is in excess of 3,100° C. After the tube was mostly sealed, only leaving a very narrow channel in the glass, a vacuum pump was attached to the open end of the vessel and active vacuum was applied. When a pressure on the order of 10^{-4} Torr was attained, the torch was reapplied to the glass, closing the small channel and completing the seal. The vessel was then checked to ensure no leaks were present and then subjected to the heat treatment protocol. Special care was taken to not over fill the tube with powder as the material vaporizes during the heat treatment, thus changing the pressure inside the tube and potentially creating too much pressure for the seal to contain, resulting in mechanical failure of the glass.

Both vessels provided sufficient atmosphere for the reaction to occur but provided different results. This difference is attributed to oxygen levels present inside of the reaction vessel. The target environment for the reaction was vacuum on the order of 10^{-4} Torr, but the first vessel had a slight leak because of the mechanical compression fit that consisted of rubber O-rings and brass fittings that provided the compression. The leak was small, but enough to change the base pressure over the ninety-six-hour reaction. This was the main driver to use a different sealing method. Oxidation measured in XPS and XRD analysis was originally attributed to the nature of chromium and its oxidation at elevated temperatures. Because of this, special care was taken to keep all samples under active vacuum as much as possible. In order to avoid this oxidation, a second sealing method was developed and employed with the goal of avoiding oxidation between synthesis and analysis. Only after analyzing the sample reacted in the second reaction

vessel was it determined that the oxygen present in the first vessel had an effect on final formation.

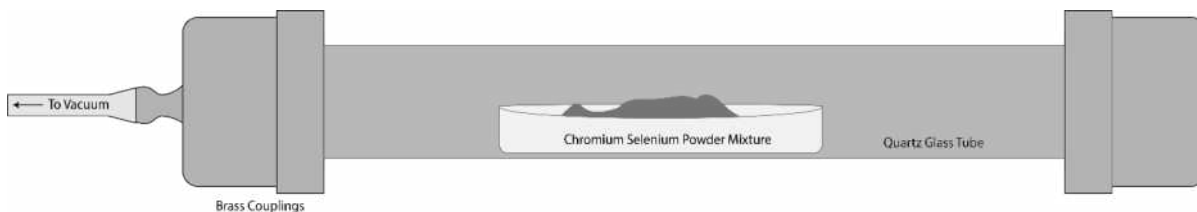


Figure 2.1: Schematic of Reaction Vessel 1 with powder sample.

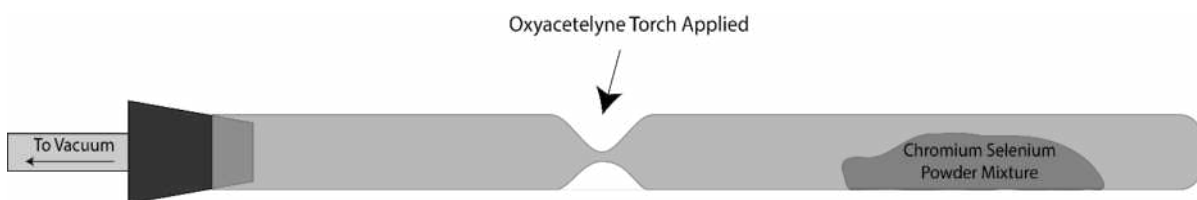


Figure 2.2: Schematic of Reaction Vessel 2 with powder sample.

2.2 Heat Treatment

After sealing, the reaction vessels were then placed in a high temperature tub furnace and heated to 500° C for 24 hours. The temperature was then increased to 800° C for an additional 96 hours before cooling naturally to room temperature. This heat treatment was carried out in a Lindberg-Blue high temperature tube furnace contained in a fume hood. A fume hood was used because selenium vaporizes at 685° C and selenium gas can be toxic in high concentrations, in the event the reaction vessel ruptured, or selenium gas was present in the vacuum exhaust, the fume hood would filter the selenium and maintain a safe working environment. The heat treatment method was similar to the method used to produce molybdenum disulfide mono layer

materials.¹⁹ The method used was adapted to serve as a generalized method of producing transition metal chalcogenides. This method was previously used within the group to produce various chromium sulfur compounds and since the melting points of chromium and selenium are fairly close to each other, the treatment protocol was not altered for selenium use. Although this method may not be a completely generalized method for all transition metal chalcogenides, it has been shown to work for at least two combinations of chromium chalcogenides, suggesting it may be a quasi-general heat treatment for some of the numerous transition metal chalcogenides.

2.3 Deposition on Sapphire

After initial analysis, a small amount of the synthesized powder was deposited on a clean sapphire substrate via solid vapor deposition. The powder was placed in a sealed quartz tube and purged with argon before pulling vacuum. Base pressure on the order of 10^{-5} Torr was achieved before continuing. The furnace was then heated to 850°C before the tube was introduced. The tube was then placed in the furnace and argon was used as a carrier gas, maintaining a pressure of 2 Torr for a 30-minute deposition. The powder was placed in the middle of the tube to ensure it would be placed in the middle of the furnace, thus experiencing the highest and most uniform heat. The clean substrate was mounted near vertical using a tungsten support to ensure a large surface area for deposition. The substrate was placed at the edge of the tube, where the temperature was lower, to ensure a thermally preferred deposition site. This thermal gradient, along with the argon carrier gas, caused the particles to accumulate on the sapphire substrate. After cooling naturally, the sample was analyzed using an Atomic Force Microscope (AFM) to determine the overall size of the deposited particles. As the sample was heated, particles were emitted via thermal evaporation and carried to the cool substrate. The size of the particles is

characteristic of the material and the total substrate coverage could be altered with time. This deposition technique is aimed at growing two-dimensional or quasi-two-dimensional structures of the given material. The size and thickness of the formed structures were subsequently analyzed with atomic force microscopy.

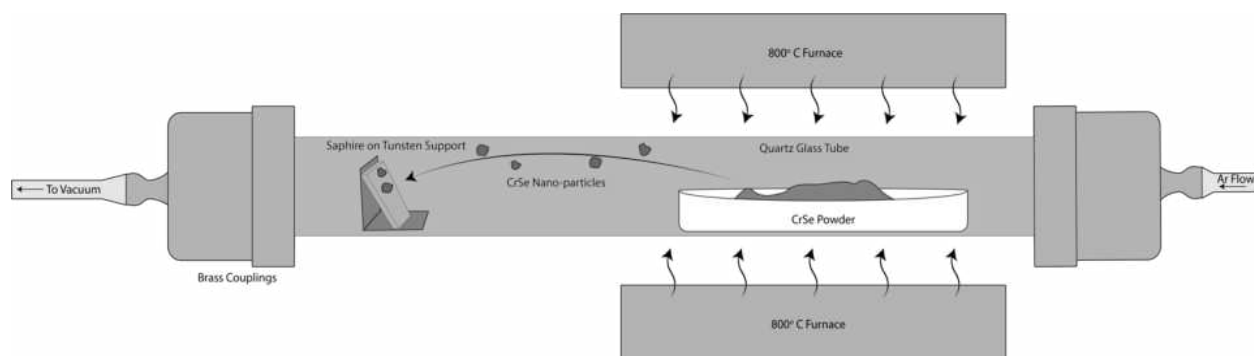


Figure 2.3: A schematic of depositing synthesized powder on to a sapphire substrate. The particles are carried by argon gas to a landing site placed just outside of the furnace.

CHAPTER III

CHARACTERIZATION TECHNIQUES

3.1 X-ray Diffraction

Powder X-ray diffraction (XRD) was used to determine which phases were present in each sample. To avoid oxidation, each sample was kept under low-vacuum until they could be transferred to the sample space. Each sample was transported in a sealed container that had been purged with nitrogen to mitigate oxidation. Powder x-ray diffraction consists of rotating an x-ray source around a powder sample and measuring the scattering as a function of incident angle. This characterization technique provides information about the crystal structure of the sample and can determine the phase of each material since each phase has a different crystal structure. Since the crystal structure of a material can be calculated, comparing the data obtained to other reported data and computational models provides a reference for our material. A Rigaku Smartlab X-ray diffractometer was used for all characterization and a copper K_{α} radiation source was used to irradiate the samples. XRD results obtained show that the resulting phase changes depending on which reaction vessel is used. Since one reaction vessel is completely sealed during the heat treatment while the other is known to have small leaks, the difference in phase formation and presence of chromium oxide can be attributed to atmospheric impurities introduced through the small leak in the vessel.

X-ray Powder Diffraction utilizes X-rays and Bragg's Law to determine parameters of crystalline materials through constructive interference. X-rays are generated within an evacuated tube using a hot filament and copper target, electrons ejected from the filament bombard the

copper target and create X-rays from the collision. Copper K_{α} X-rays are used and have an energy of 8.04 keV and thus a wavelength of 1.54 Å. These X-rays are passed through a monochromator and collimator to provide a coherent beam of X-rays and directed to the sample space. The sample must be in powder form and have a small particle size to allow for homogeneity and a sufficient distribution of crystal structures. Because the sample is in powder form, the angle of any given crystal structure is random and thus the source and detector are swept through an angular range to satisfy conditions of Bragg's equation. The incident X-rays will reflect off of crystalline planes and either interfere constructively or destructively depending on the angle of incidence. Thus, as the X-ray source and detector are swept through the appropriate angles, the intensity of detected X-rays changes as a function of incident angle theta. These maxima correspond to the constructive interference predicted by Bragg's Law and thus the inter-atomic distances can be calculated since the wavelength and angle are known parameters. The resulting inter-atomic spacing information can be used to identify the material present in the sample by consulting a database, which is typically included in the analysis software.

3.2 X-ray Photoelectron Spectroscopy

X-ray photoelectron spectroscopy (XPS) was used to determine chemical bonding within each sample. After each sample was analyzed with XRD, each powder was pressed into a thin indium foil and affixed to an XPS stub via carbon tape. Indium foil was used to secure the powder to the sample stub because of the nature of sample entry into the ultra-high vacuum (UHV) system. Not only can the actuation of valves and pressure differences disturb loose powder, the sample stub must also be inverted to secure to the transfer arm mechanism. This makes analyzing loose powder impractical and thus a soft metal was used to keep the powder in place. Indium was used

because of its malleability at room temperature, simply placing powder on top of the metal and pressing will embed the powder into the foil and allow inversion without losing any material. In many cases, enough powder was used as to diminish or entirely suppress the indium peaks from the survey. Since XPS is a highly surface sensitive characterization technique, on the order of 10 nm, As a result, only a few layers of powder was sufficient to completely cover the indium signal from analysis. The XPS system used consisted of a non-monochromated X-ray beam generated from an aluminum source and operating at 300 Watts and a base pressure of 1×10^{-10} Torr. Survey scans of each sample were acquired to determine the overall composition and obtain a chromium to selenium ratio. Higher resolution multiplex scans were used to measure chromium 3p and 3s peaks as well as selenium 3p peaks. Multiplex scans have fine enough resolution to quantitatively assess and assign any shift in the XPS peaks due to physical and chemical conditions of the investigated element.

XPS analysis consists of bombarding a sample surface with high energy X-rays and subsequently capturing the emitted electrons that have been ejected via the photoelectric effect. X-rays are generated by heating a filament that excites electrons and subsequently bombards an aluminum or magnesium target, collisions with the aluminum target create Al K_{α} X-ray radiation at 1486.6 eV. These X-rays are then focused on to the sample where they are able to eject core electrons. The number of X-rays per unit time, or the flux, is determined by the operating conditions of the system, the XPS used for all experiments was operated at 300 Watts for every test, as this gives a sufficient amount of X-ray flux. If the energy of the incoming X-ray exceeds the energy of the work function and binding energy of the electron, any excess energy is transferred to the electron in the form of kinetic energy, the electron then travels toward the

detector where the velocity is measured via a hemispherical analyzer. Thus, if the work function of the detector is known, then the kinetic energy of the electron directly corresponds to the binding energy of the electron, which would be the energy of the incident X-ray, less the work function of the sample and kinetic energy of the electron. The hemispherical analyzer sweeps the detection range from 1486.6 eV to 0 eV at a predetermined step size to determine the relative electron counts at each energy value and thus providing intensity as a function of binding energy. Each element has unique binding energies due to their electron configurations. The core electrons are affected by the photoelectric effect, the output data can be used to match binding energies and determine the chemical composition of the sample. Depending on the chemical binding, the peaks may shift to higher or lower binding energies and can be compared to experiment to determine exact sample characteristics. In general, oxidation will force binding energies to higher values which can be determined by analyzing the output data. Every sample that is not prepared in UHV or sputtered will contain oxygen and carbon contamination. Since these peaks will always be present they can be used as a calibration mechanism to ensure the system is reading properly. The carbon 1s peak will always occur at 285 eV while the oxygen 1s peak will occur at 531 eV. Since both samples were momentarily exposed to atmosphere, both carbon and oxygen are present and can be used to ensure the sample did not charge. A sample can accumulate a charge if it is not sufficiently conducting. Because the XPS works by ejecting electrons from individual atoms, if the sample does not conduct well, the vacancies cannot be filled thus creating excess positive charge on the sample and making it increasingly difficult to remove additional electrons. This phenomenon can be easily detected as most non-metallic samples, the peaks will shift to higher binding energies and become broader as the scan

continues. After checking the results and determining neither sample experienced charging, analysis was continued without any special charge compensation considerations.

Following are schematics of both the analysis chamber of the XPS where an X-ray beam is focused on the sample and ejected electrons are collected by the detector where the energy is then obtained by measuring the velocity of the ejected electron. The angle of the X-ray source and detector are fixed, and the sample may be translated via a three-way manipulator that extends out of the vacuum chamber. Because the spot size of the beam is 10-15 mm in diameter, the data obtained is not spatially confined, but the beam only effects the first 10 nm of the sample, so the technique is extremely surface sensitive.

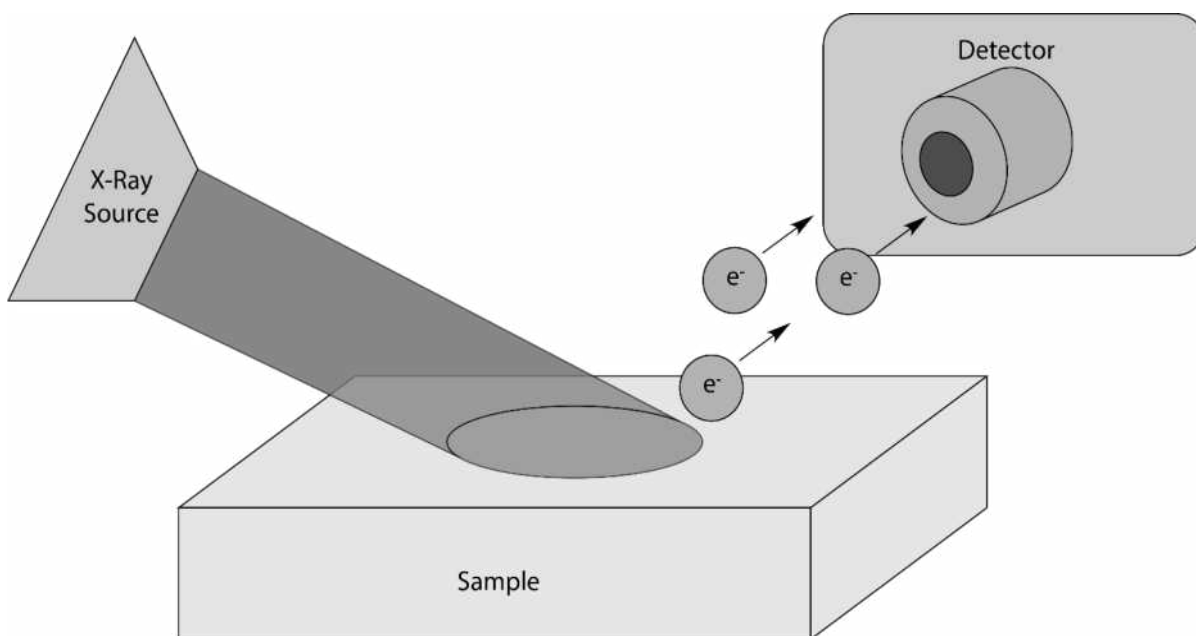


Figure 3.1: Schematic of an XPS, an X-ray beam is focused on the sample and ejected electrons are collected by the detector.

The XPS generates X-rays that are then used to bombard the sample surface via an internal X-ray source, a hot filament excites electrons that then bombard the positively charged aluminum target. The collision then emits X-rays that are directed through magnetic lenses toward the sample space. This interaction produces Al $K\alpha$ radiation with an energy of 1486.6 eV. This source is water cooled to handle the large amount of power dissipated from the X-ray generation process. A thin aluminum foil separates the targets from the sample space as to avoid contamination and protect the sample from stray radiation. This foil is permeable by the X-rays but blocks stray particles from interacting with the sample space and conversely protects the targets from sample contamination in the event that some of the sample is dislodged from the sample stub.

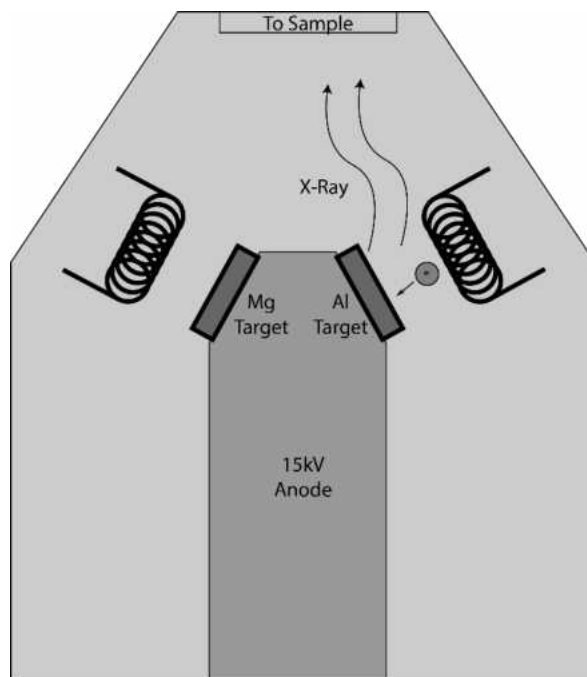


Figure 3.2: Schematic of the X-ray source, a filament is heated and excites an aluminum target that in turn generates x-rays that are then focused using electromagnetic lenses and focused on the sample.

3.3 Atomic Force Microscopy

After depositing a small amount of powder on a clean sapphire substrate, the sample was immediately affixed to an AFM sample stub and analyzed. Atomic Force Microscopy employs a rastering cantilever that scans the surface and reports topographical as well as amplitude and phase information. This information gives insight into the types of structures formed by the deposition and the overall height of these structures. The final topographical image can be processed, and height measurements can be made, from which, the number of layers can be inferred. A Nanomagetics ezAFM Atomic Force Microscope was used for all AFM measurements. The AFM was operated in tapping mode for all scans. The scan head was mechanically isolated using inertial damping through a spring system and additionally isolation through an air suspension system. The combinations of these two systems allowed maximum scan resolution to be attained.

Atomic Force Microscopy utilizes a small cantilever that rasters across the sample surface. As a result, the sample surface must be flat enough to avoid damaging the tip. AFMs can be operated in various modes depending on the tip used. Contact mode tips involve direct contact with the sample surface, whereas tapping mode operates with a sharp tip, typically made of silicon vibrating above the sample surface. Tapping mode tips never actually contacts the sample surface, rather it responds to the repulsion between atoms. A laser is directed to the back of the cantilever and the reflected beam is measured via a photodiode. As the tip is moved across the sample, the sample topography can be obtained as a function of position. Because the tip is driven at a specified frequency, any changes in the amplitude or phase of this frequency can be used to obtain characteristics of the sample surface.

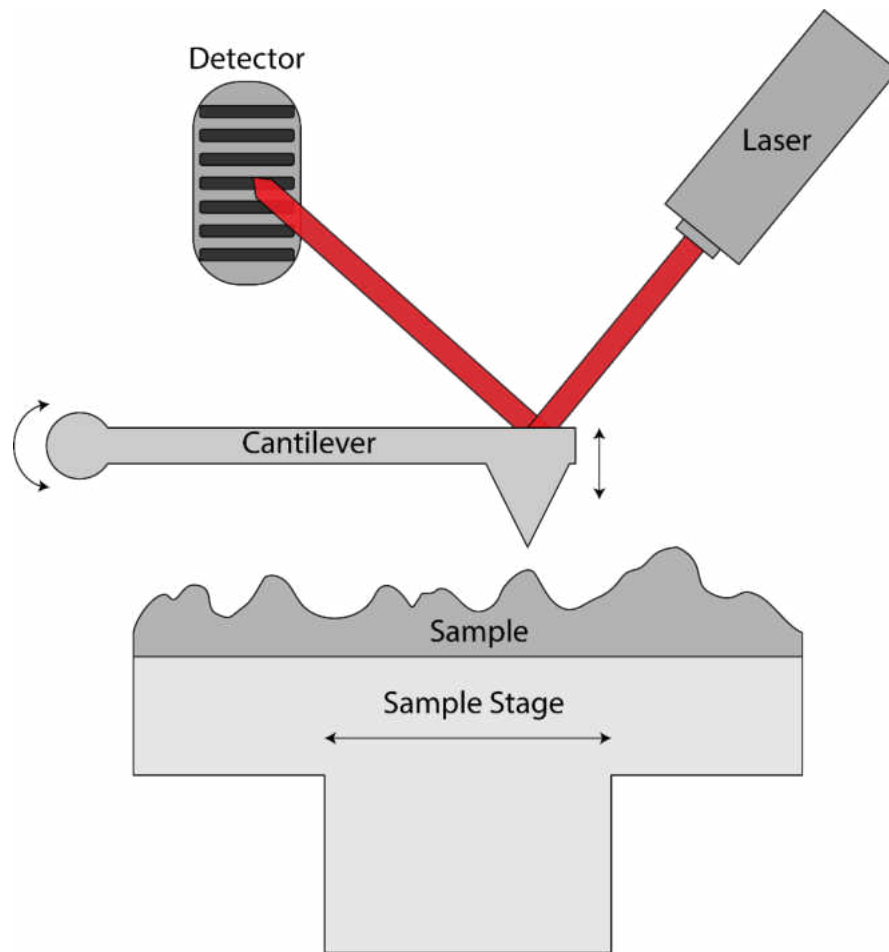


Figure 3.3: Schematic of AFM scan head, a cantilever rasters across a sample and as the tip moves up and down, a laser focused on the top of the cantilever changes position. The reflection of the laser is detected via a photodetector and topography data is obtained.

CHAPTER IV

RESULTS AND DISCUSSION

4.1 X-ray Diffraction Analysis

Immediately after synthesis, each sample was analyzed via powder X-ray diffraction to determine the crystal structure of the powder. Sample 1, the sample reacted in the first type of reaction vessel, was determined to be Cr_3Se_4 but also contained chromium oxides. This was an indicator that either our sample was oxidizing in route to the characterization equipment or that the reaction vessel itself contained a leak, thus oxidizing the sample. The next step was to either develop a new reaction vessel to limit oxygen content during the reaction. Because the mechanical couplings may have introduced oxygen into the system, the decision was made to eliminate them from the set up. This was accomplished by completely sealing a section of glass tube that contained the reaction materials while under active vacuum. After synthesizing a new sample, Sample 2, with the new reaction vessel, the powder was again analyzed via XRD and the expected result was to obtain a pure phase of the previous material. However, the XRD data showed that Sample 2 was Cr_2Se_3 . The transition from Cr_3Se_4 to Cr_2Se_3 was apparent because the two compounds have different crystal structures, thus producing different XRD patterns.

XRD results for each sample were used to determine the crystal structure and composition of each sample. Sample 1 was determined to be a mixed phase of Cr_3Se_4 , Cr_2O_3 , and CrO in 57.3, 33.7, and 9.04 weight percentages, respectively. The crystal structure of each component was also determined. The Cr_3Se_4 crystal structure was determined to be in the $C2/m$ space group which is a monoclinic crystal structure. Sample 2 was found to be a much purer phase with

relative concentrations of Cr_2Se_3 and elemental Se in 76.9 and 23.1 weight percentages respectively. Sample 2 was determined to be in the $R\bar{3}$ space group which is a trigonal crystal structure.

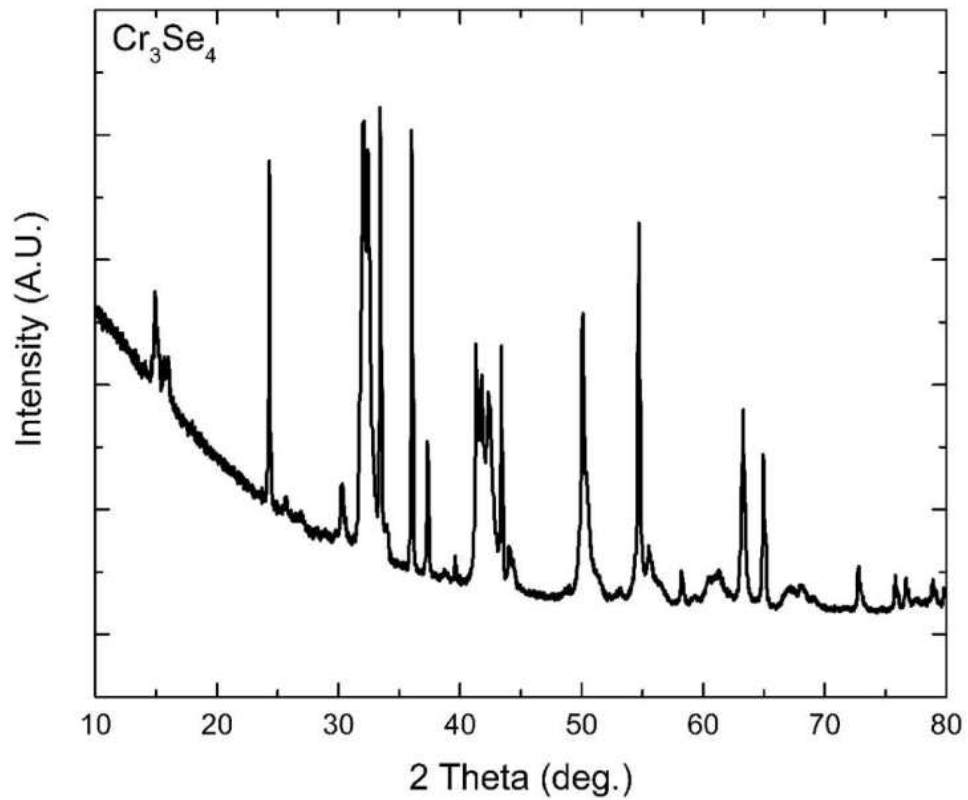


Figure 4.1: XRD results from Sample 1.

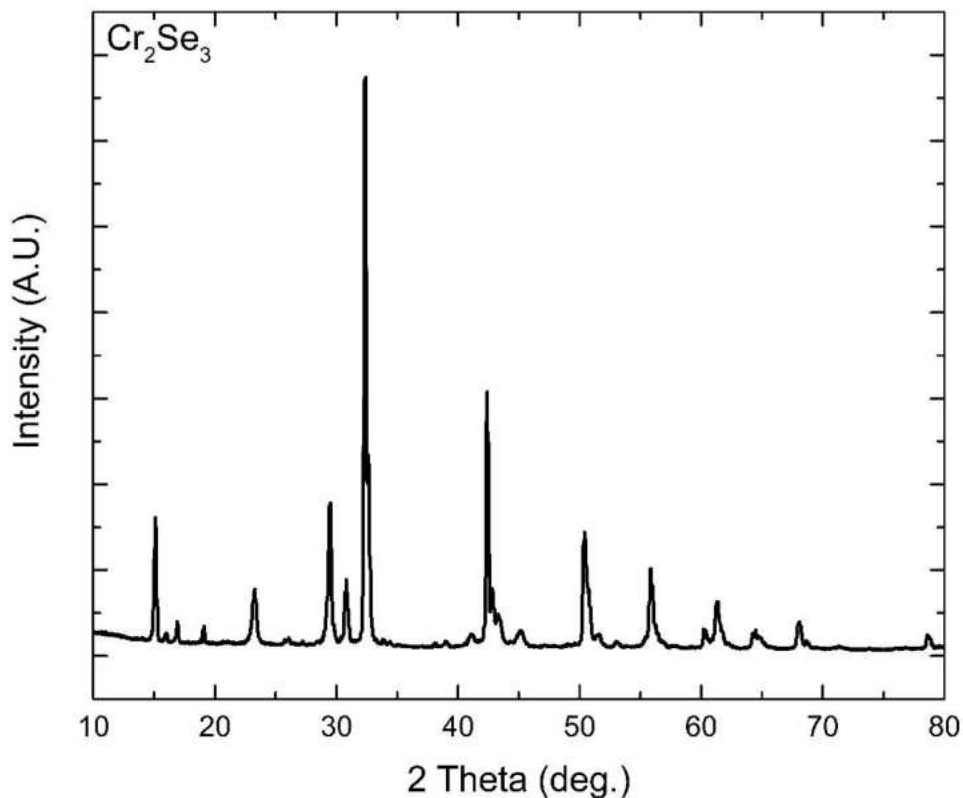


Figure 4.2: XRD results from Sample 2.

4.2 X-ray Photoelectron Spectroscopy Survey Analysis

After XRD analysis each sample was analyzed via X-ray Photoelectron Spectroscopy in order to determine chemical composition and binding within the sample. XPS surveys provide information about the overall chemical composition of the sample and the relative contents of each element. These surveys, when combined with XRD results, provide a clear understanding of the crystal structure and chemical makeup of the sample. Along with the surveys which capture the overall chemical contributions with relatively low resolution, high resolution multiplexes

were also obtained for each sample, focusing on the chromium $3p_{1/2}$, $3p_{3/2}$, and $3s$ peaks as well as selenium $3d$ peak. These multiplexes provide in depth information about the bonding of each element as the energy resolution is much finer than that of a survey and multiple passes are combined to obtain a clear representation of the chemical composition. The high-resolution scans can reveal peak splitting due to multiplet splitting. Peaks will shift to higher or lower binding energies depending on how the electron orbitals interact, for example selenium has a $3d$ peak located at 57 eV but when selenides are present the binding energy of the $3d$ peak will shift to 54-55 eV.

Peak splitting can also occur and is best resolved through multiplex analysis, these mechanisms are divided into spin-orbit splitting and multiplet splitting. Spin orbit splitting is due to the interaction of electron spin and orbital angular momentum. The Hamiltonian contains a component that is proportional to both the magnetic moment and effective magnetic field generated by the moving charge. The magnetic moment is proportional to the spin of the electron and the effective magnetic field is proportional to orbital angular momentum via Biot-Savart's law. Since the spin orbit coupling contribution to the energy is proportional to the orbital angular momentum, the term vanishes when the orbital angular momentum is zero, or the electron is in the s orbital. Thus, spin orbit coupling is only present in the p , d , and f orbitals.^{20,21}

Multiplet splitting (or exchange splitting) happens when photoionization creates an unpaired electron in one of the core levels. This unpaired electron in the core shell couples with unpaired valence electrons. The effect of the coupling on the binding energy depends on the spin combinations of the unpaired electrons. This phenomenon exhibit itself in the XPS as a peak

splitting. Unlike spin orbit splitting, multiplet splitting can change the binding energy of any electron from any core level, including s orbitals.

The surveys of Sample 1 and Sample 2 confirm the presence of chromium and selenium in each sample but because there is unreacted selenium in Sample 2, quantitative determinations of ratios cannot be made via XPS analysis and should rather be obtained via the crystal structures found in XRD analysis. In Figures 4.3 and 4.4 a number of unlabeled peaks are present; these peaks are indium peaks originating from the indium foil the sample powder is pressed into. They are not labeled because they give no useful chemical information pertaining to the sample. Sample 1 has a carbon 1s peak at 285 eV and Sample 2 has a carbon peak at 284.5 eV and thus dispels any concern about charging during analysis. Sample charging occurs when the sample has insulating properties and cannot fill vacant electron orbitals, thus accumulating a net positive charge and making additional electron ejections increasingly difficult, which appears as a shift to higher binding energies. Since neither sample is accumulating a charge during the analysis, all shifts in binding energy can be attributed to either oxidation or chemical bonding.

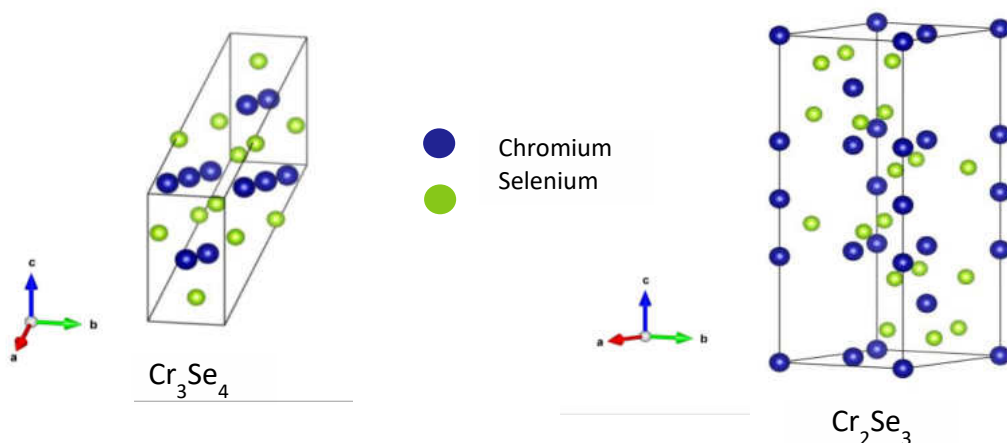


Figure 4.3: Crystal structures of Cr_3Se_4 and Cr_2Se_3 .

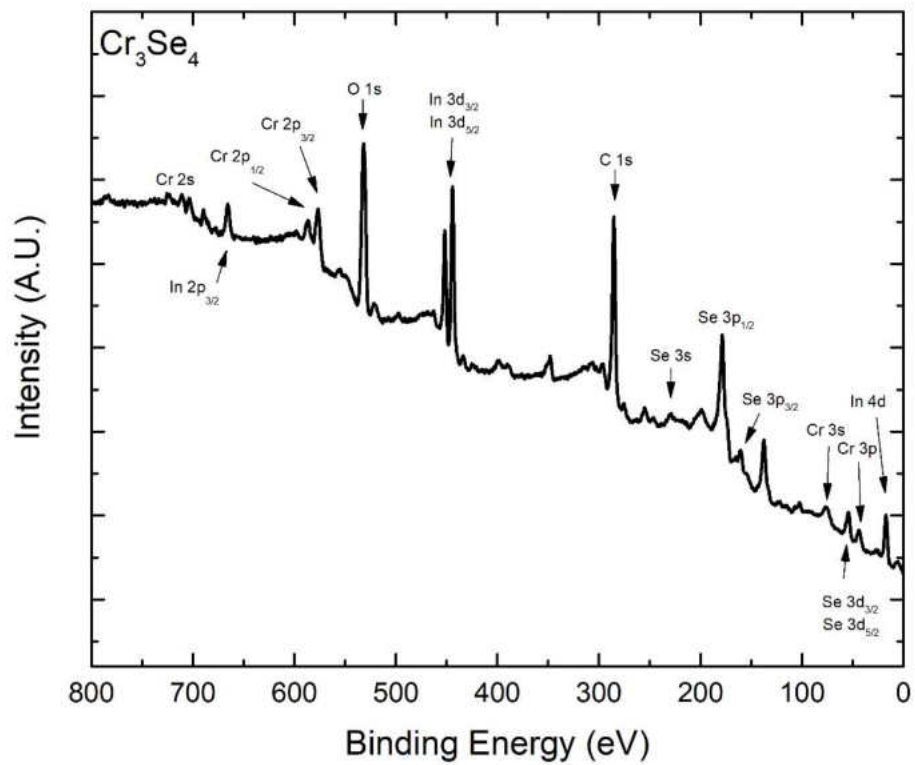


Figure 4.4: XPS survey of Sample 1.

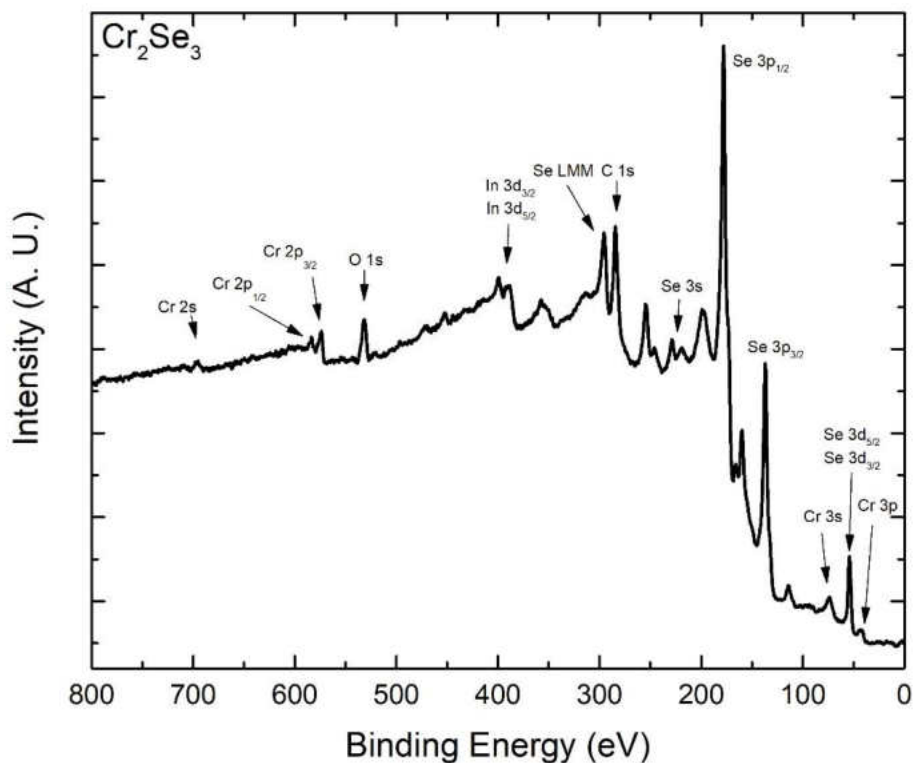


Figure 4.5: XPS survey of Sample 2.

4.3 X-ray Photoelectron Spectroscopy Multiplex Analysis

High resolution multiplex scans were acquired for various chromium and selenium peaks for both Sample 1 and Sample 2, denoted as Cr_3Se_4 and Cr_2Se_3 respectively. These scans encompass a much smaller energy window and have a much finer step size, allowing a quantitative analysis of peak splitting due to spin orbital splitting or multiplet splitting. Multiplex scans were acquired for the chromium 2p and 3s peaks as well as the selenium 3d peaks for both samples. These peaks were chosen because they are the most prominent and give insight into the chemical state of each element. Each peak should occur at a specific energy level and using accepted data, determinations on binding or oxidation can be made. The chromium 2p is affected by spin orbit

splitting and multiplet splitting induced by the spin combinations of the p orbital electrons. The elemental chromium 2p peak is resolved into a $2p_{3/2}$ peak at 574 eV and a $2p_{1/2}$ peak at 583 eV with a reported energy difference of 9.2 eV.²² This energy difference is not affected by charging as each contribution will undergo the same amount of charging, leaving the relative difference unchanged. Elemental chromium also has a characteristic peak from the 3s orbital at 75 eV that exhibit multiplet splitting under the right conditions.^{23,24}

The chromium 2p peak for Sample 1, Cr_3Se_4 , has a $2p_{3/2}$ contribution at an energy of 576.6 eV and a $2p_{1/2}$ contribution at 587.6 eV, giving an energy difference of 11 eV. The position of the first peak is in line with what is expected of Cr_2O_3 as reported.²² However, the energy difference is significantly higher than the one for both elemental chromium (9.2 eV) and Cr_2O_3 (9.8 eV). This difference can be attributed to the fact that Sample 1 has complicated chemistry and changes in the local chemistry affect the multiplet splitting.²³ For Sample 2, Cr_2Se_3 , the $2p_{3/2}$ and $2p_{1/2}$ contributions are at 573.6 eV and 583.2 eV respectively. This agrees with the only reported peak positions for Cr_2Se_3 of 574.5 eV and 584.1 eV.²⁵ The measured peaks are almost 1 eV lower than the reported values however, the difference between $2p_{3/2}$ and $2p_{1/2}$ are the same. The 1 eV difference can be attributed to the calibration of XPS on the carbon peak.

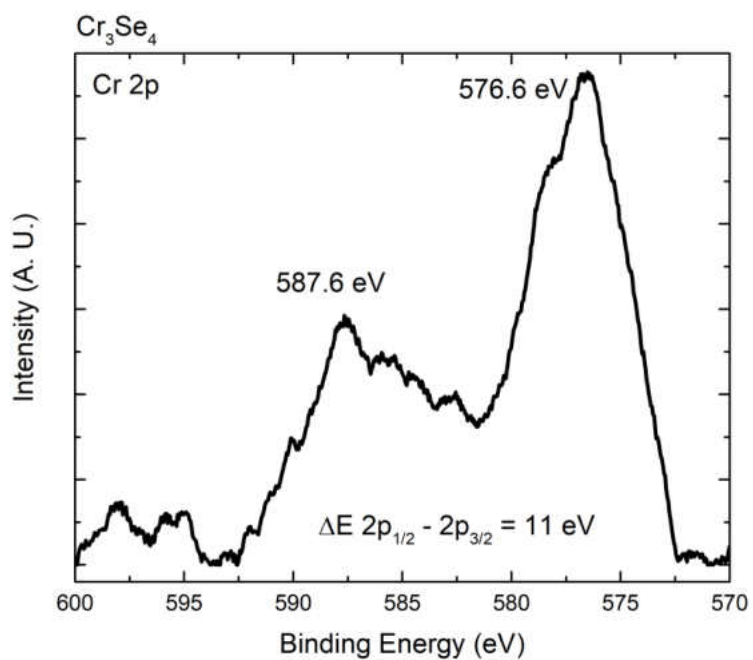


Figure 4.6: Multiplex of Sample 1 Cr 2p peak.

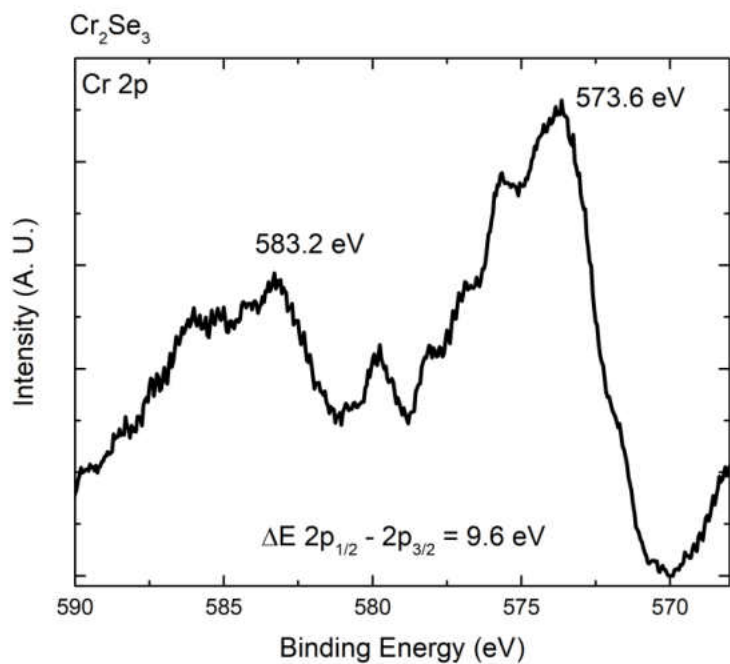


Figure 4.7: Multiplex of Sample 2 Cr 2p peak.

For elemental chromium, the 3s peak is at 75 eV. Due to multiplet splitting in Sample 1, Cr_3Se_4 , the 3s peak becomes a doublet and has two components, one at 76 eV and the other occurring at 73 eV. In Sample 2, Cr_2Se_3 , multiplet splitting can reveal itself as the peak broadening. This multiplet splitting is not resolved into two independent peaks, rather it is comprised of two broad peaks that together, construct the observed 3s peak. The shifts observed in Cr 3s peaks is worth noting and need further investigation.

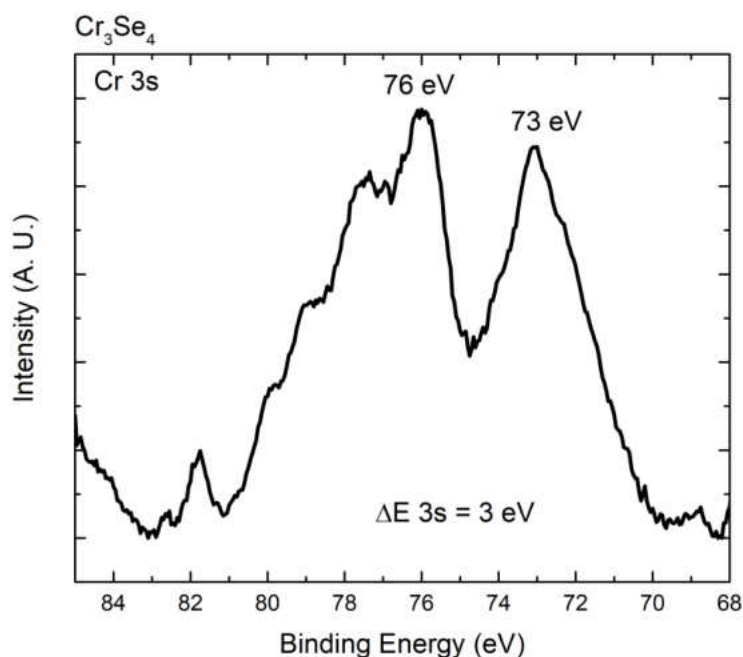


Figure 4.8: Multiplex of Sample 1 Cr 3s peak.

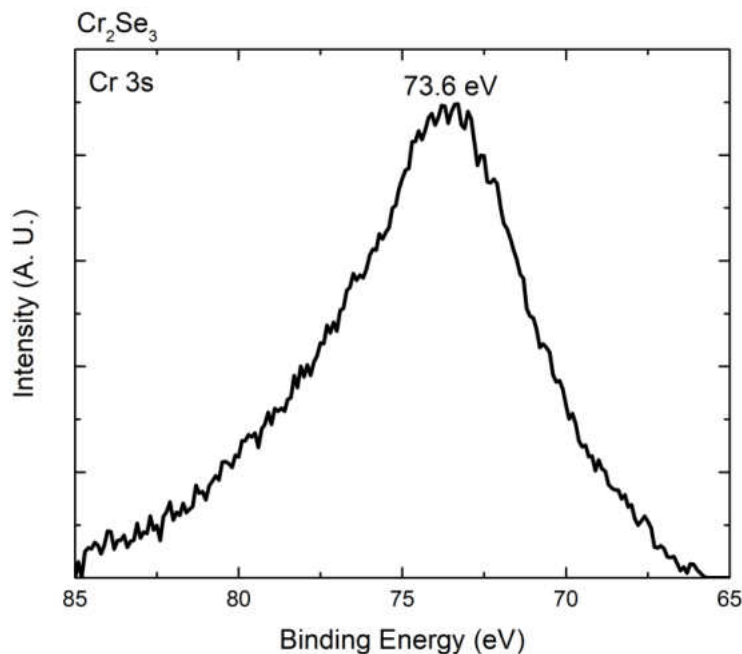


Figure 4.9: Multiplex of Sample 2 Cr 3s peak.

Multiplex scans of the selenium 3d peak for each sample both occur at within 0.1 eV of 54 eV, which is 2 eV lower than the expected result for elemental selenium. However, the Perkin-Elmer Handbook of Photoelectron Spectroscopy reports the binding energy of selenium shifts to a lower value when in the selenide form. Therefore, it would appear the measured spectra confirm the presence of selenides in the sample, confirming the XRD analysis previously discussed. More apparent in the Sample 1, Cr₃Se₄, multiplex is a peak broadening or shoulder on the higher energy side of the peak. This is due to the d orbital spin orbital splitting, but since the energy difference between Se 3d_{5/2} and Se 3d_{3/2} is only 0.86 eV, the individual peaks cannot be resolved. The XPS in the lab is not monochromatic and therefore has a large full width half maximum.

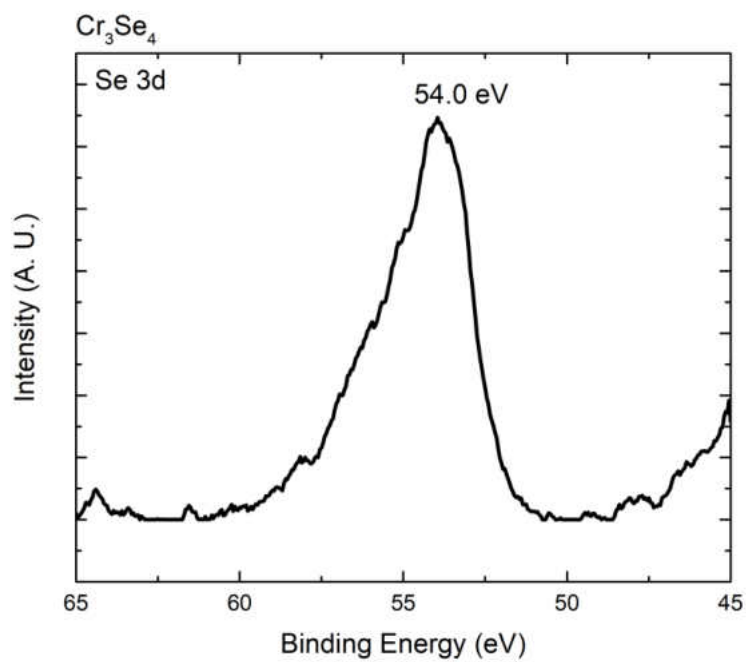


Figure 4.10: Multiplex of Sample 1 Se 3d peak.

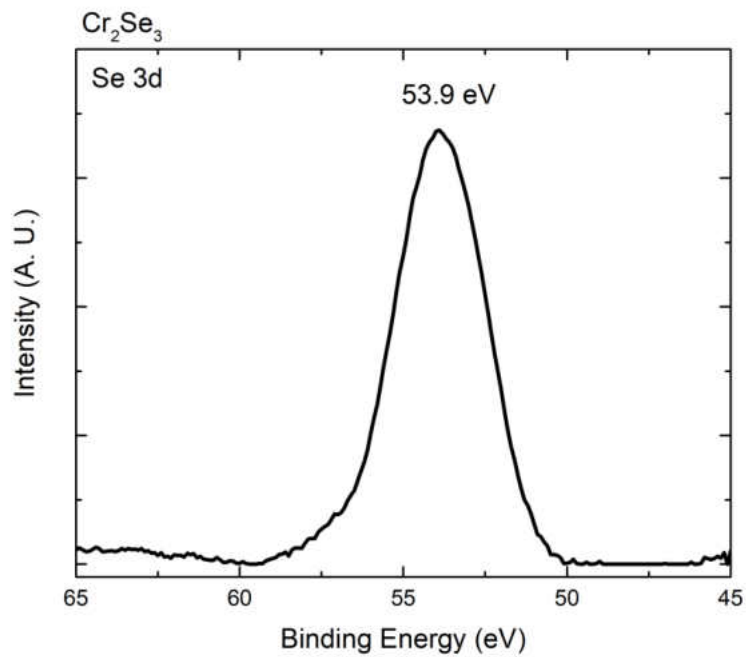


Figure 4.11: Multiplex of Sample 2 Se 3d peak.

4.4 Atomic Force Microscopy Analysis

After each sample had been characterized with XRD and XPS techniques, a small amount of powder was placed into Reaction Vessel 1 and annealed at 800° C for 30 minutes under argon flow at a pressure of 2 Torr. Along with the powder, a sapphire substrate propped up on a tungsten support was placed within the reaction vessel but outside of the furnace. This effectively created a thermodynamically preferable landing site for any particles that were evaporated and carried by the argon gas. After the 30-minute deposition was finished, the furnace was turned off and argon continued to flow at the same rate until the furnace cooled naturally to ambient temperature. This procedure was performed for both Sample 1 and Sample 2, each sample was analyzed via atomic force microscopy to determine if either sample produced two-dimensional or quasi-two-dimensional materials. Sample 1 displayed structures that were 5-25 nm in height and 2 μm across with a consistently circular shape. As mentioned above, sample 1, Cr_3Se_4 mixed phase, and Sample 2, Cr_2Se_3 , have distinct crystal structures, $C2/m$ and $R\bar{3}$ respectively.

The AFM used captured topographical, phase, and amplitude images of each sample, but the topographical images are of greatest interest for the purposes of this investigation. Topographical images can be quantitatively analyzed, and height information can be extracted through line scans of the sample surface.

Although the AFM was able to resolve particles only 5-7 nm in height, the device used was at the limit of measurement resolution and did not yield sufficiently detailed results. In order to reveal more structural information, plans to investigate powder with a Transmission Electron

Microscope (TEM) are currently in development. TEM analysis would provide a higher resolution image of the nano-structures observed in AFM analysis.

Scans from the Cr_3Se_4 mixed phase deposition show numerous circular islands with small structures that appear to preferentially form on or near the circular structures. The large circular structures are consistently on the order of $2\ \mu\text{m}$ in diameter and on the order of 5-25 nm high. Upon scanning one of the circular islands, the small formations appear to have generally amorphous shapes and are on the order of 7-10 nm high.

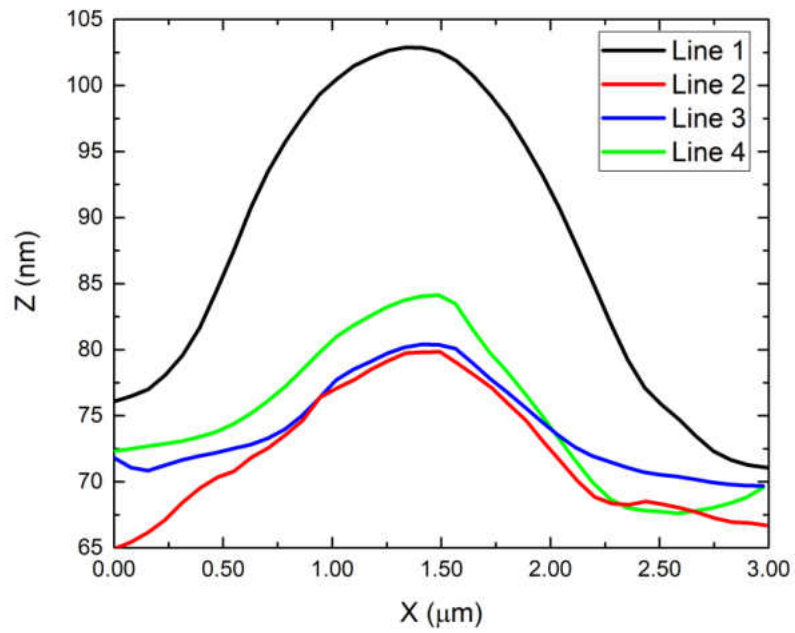
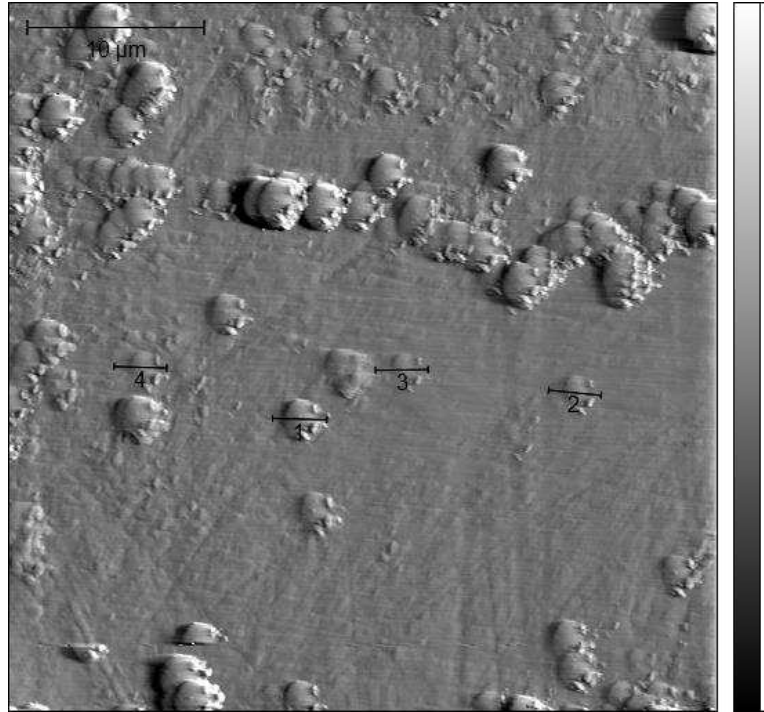


Figure 4.12: 40 μm x 40 μm topographical image and height profiles of Cr₃Se₄ powder deposited on sapphire substrate.

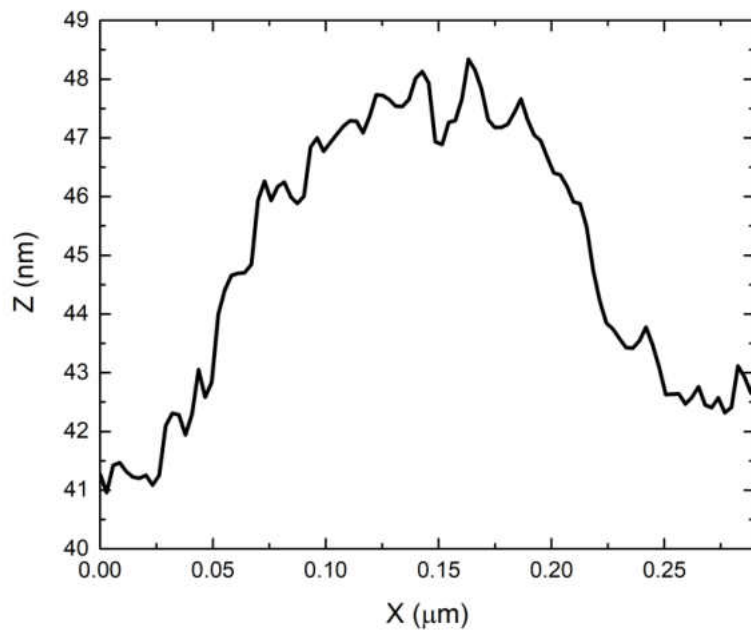
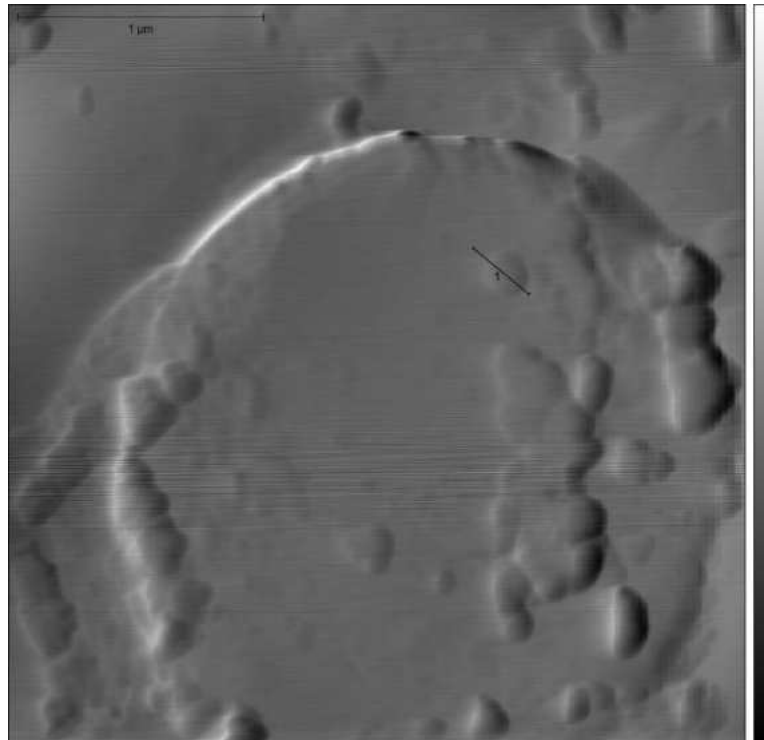


Figure 4.13: 3 μm x 3 μm topographical image and height profiles of Cr₃Se₄ powder deposited on sapphire substrate.

Scans of the Cr_2Se_3 powder deposition show a number of triangular structures present on the sapphire surface that are all oriented in the same direction. There appear to be fewer structures present on this sample than in the case of the Cr_3Se_4 deposition. Again, there are smaller amorphous structures present on the larger structures. The larger triangular structures are on the order of 1-2 μm and are on the order of 5-15 nm high. Higher magnification scans would aid in the characterization of these particles but the AFM used did not have fine enough resolution and a finer analysis technique must be used.

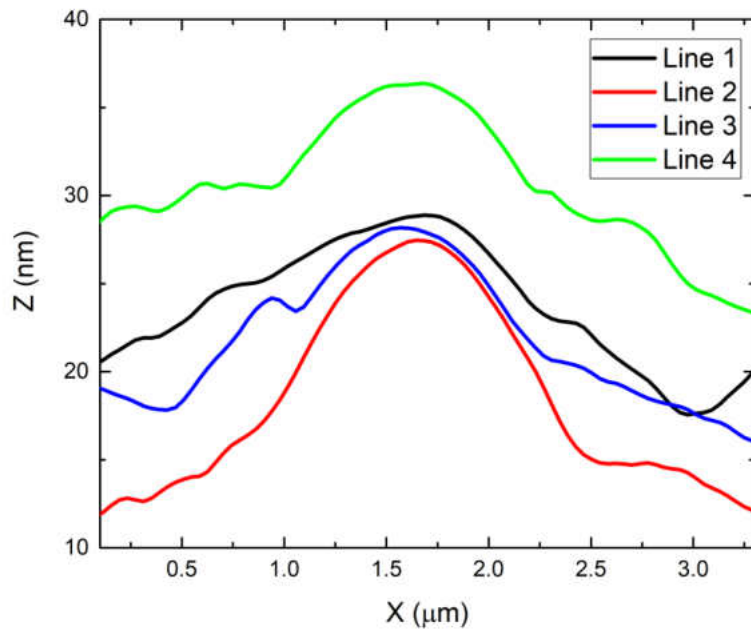
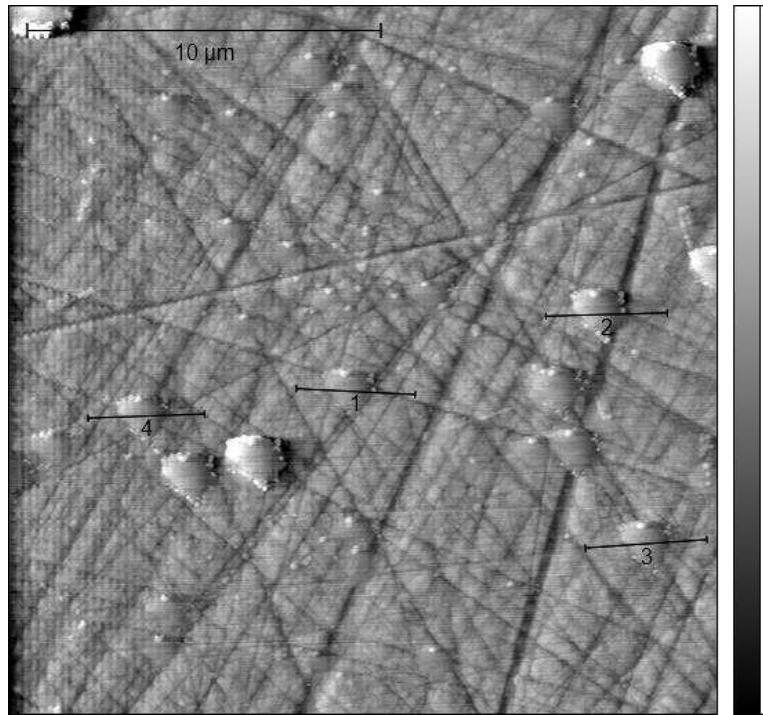


Figure 4.14: 20 μm x 20 μm topographical image and height profile of Cr₂Se₃ powder deposited on sapphire substrate.

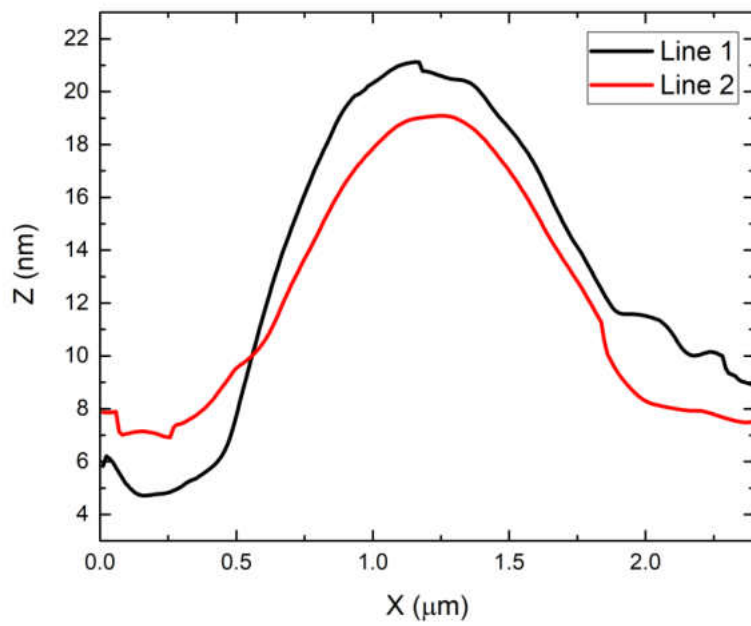
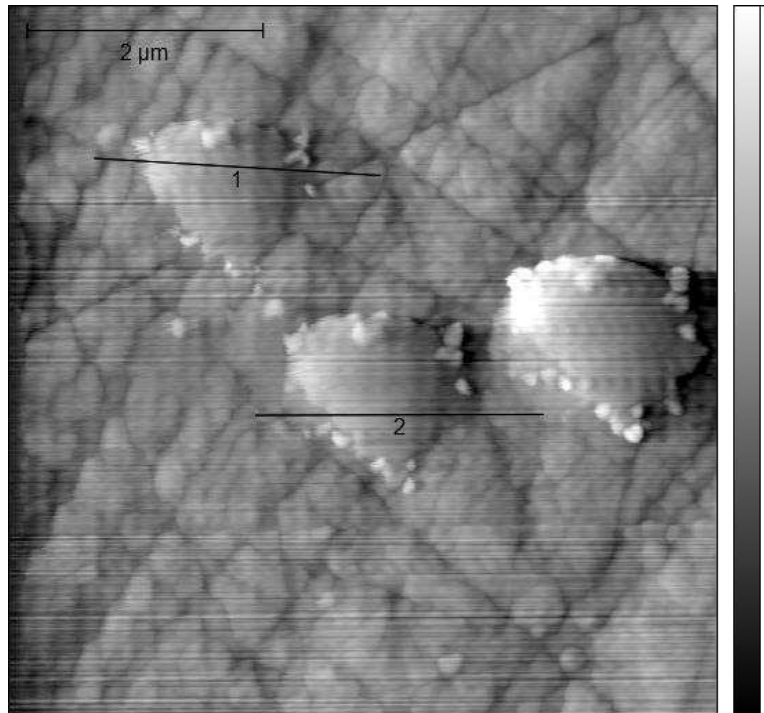


Figure 4.15: $5\ \mu\text{m} \times 5\ \mu\text{m}$ topographical image and height profile of Cr_2Se_3 powder deposited on sapphire substrate.

CHAPTER V

CONCLUSION

Chromium and selenium powders were combined in a 2:3 ratio in evacuated reaction vessels and the resulting composition varied as the reaction vessels were interchanged. This result is attributed to the oxygen content within each reaction vessel during heat treatment. Because the first reaction vessel was shown to have sealing issues during testing a second permanently sealed reaction vessel was developed with the understanding that the oxygen contamination would be mitigated. Rather, the composition of the resulting powder changed as well, indicating that oxygen is a critical factor in final composition. Several quantitative analysis techniques were used to determine the exact composition and physical characteristics of each product. Primary conclusions are drawn from XRD and XPS data, obtaining both the crystal structure and chemical composition respectively. XRD was able to identify the compounds present in each powder where XPS was able to quantitatively assess chemical bonding within each sample. XPS surveys provided chemical composition of the entire sample whereas XPS multiplexes were acquired to analyze shifts in binding energies and peak splitting resulting from bonding. AFM was used to determine the height of deposited nano-particles but the resolution of the measurement techniques was not great enough to detect the smallest particles thus additional characterization is required.

Future considerations should include Transition Electron Microscopy (TEM) analysis to better characterize the structure of the nano-particles that were characterized with AFM. The AFM used did not acquire data at a high enough resolution to make determinations on the crystal

or atomic structure of the sample. This is problematic for Sample 1 as it is a mixed phase of both Cr_3Se_4 and oxide contaminants, thus with the acquired data, the particles cannot definitively be classified, and additional characterization is required. Another direction that is of interest in this project is titration of oxygen during the reaction, it has been shown that oxygen is a critical factor in composition and the natural question would ask how much oxygen is required to turn the reaction from one composition to the other. Although this task is conceptually very straight forward, the experimental design is challenging. Developing an oxygen introduction mechanism is the first aspect that needs to be resolved, any mechanism must be tunable and have direct access to the sample space yet be able to maintain vacuum while introducing quantifiable amounts of oxygen. Although technically challenging, this is a very interesting aspect of the experiment that warrants further investigation.

Results from this investigation should be helpful in assessing the production and characterization of some transition metal chalcogenides and hopefully sheds light on a quasi-general method for producing small scale TMC powders that can be scaled for industrial use.

REFERENCES

1. Guo, Q. & Mori, T. Thermoelectric Properties of Chromium Selenides. *J. Phys. Conf. Ser.* **1052**, 012128 (2018).
2. Jellinek, F. Transition metal chalcogenides. relationship between chemical composition, crystal structure and physical properties. *React. Solids* **5**, 323–339 (1988).
3. Adachi, Y. *et al.* Magnetic structure of rhombohedral Cr₂Se₃. *Journal of the Physical Society of Japan* **63**, 1548–1559 (1994).
4. Wehmeier, F. H., Keve, E. T. & Abrahams, S. C. Preparation, structure, and properties of some chromium selenides. Crystal growth with selenium vapor as a novel transport agent. *Inorg. Chem.* **9**, 2125–2131 (1970).
5. Matthews, P. D., McNaughter, P. D., Lewis, D. J. & O'Brien, P. Shining a light on transition metal chalcogenides for sustainable photovoltaics. *Chem. Sci.* **8**, 4177–4187 (2017).
6. Jiang, H. *et al.* 2D monolayer MoS₂--carbon interoverlapped superstructure: engineering ideal atomic interface for lithium ion storage. *Adv. Mater.* **27**, 3687–3695 (2015).
7. Snyder, G. J., Caillat, T. & Fleurial, J.-P. Thermoelectric Properties of Cr₃S₄-Type Selenides. *MRS Online Proceedings Library Archive* **545**, (1998).
8. Maurer, A. & Collin, G. Structural and physical properties of Cr₃Se₄ (x ≤ 0.20). *J. Solid State Chem.* **34**, 23–30 (1980).
9. Jain, A. *et al.* The Materials Project: A materials genome approach to accelerating materials innovation. *APL Mater.* **1**, 11002 (2013).
10. Hayashi, A. *et al.* Cation distribution in (M, M'')₃Se₄. I. (Cr, Ti)₃Se₄. *J. Solid State Chem.* **67**, 346–353 (1987).
11. Chevreton, M. & Bertaut, E. F. Etude de seleniures de chrome. *Comptes Rendus Hebd. des Seances l'Academie des Sci. (1884 - 1965)* **253**, 145–147 (1961).
12. Blachnik, R., Gunia, P. G., Fischer, M. & Lutz, H. D. Das System Chrom-Selen. *J. Less-Common Met.* **134**, 169–177 (1987).
13. Ueda, Y. *et al.* Phase diagram and metal distribution of the (Cr_xTi_{1-x})₃Se₄ system (0 = x = 1) with the Cr₃S₄ - type structure. *J. Solid State Chem.* **56**, 263–267 (1985).
14. Ohta, S., Adachi, Y., Kaneko, T., Yuzuri, M. & Yoshida, H. Thermal expansion in chromium chalcogenides Cr₂X₃ (X = Se, Te). *J. Phys. Soc. Japan* **63**, 2225–2230 (1994).
15. Boscher, N. D. *et al.* Synthesis and charaterisation of chromium oxyselenide (Cr₂Se_{0.702.3}) formed from chemical vapour synthesis: A new antiferromagnet. *Eur. J. Inorg. Chem.* **2007**, 4579–4582 (2007).
16. Chu, J. *et al.* Sub-millimeter Scale Growth of One-unit-cell Thick Ferrimagnetic Cr₂S₃

- Nanosheets. *Nano Lett.* (2019).
17. Chevreton, M., Murat, M., Eyraud, C. & Bertaut, E. F. Structure et conductibilité électrique des composés à lacunes ordonnées du système chrome-sélénium. *J. Phys.* **24**, 443–446 (1963).
 18. Kariper, I. A. Synthesis and characterization of CrSe thin film produced via chemical bath deposition. *Optical Review* **24**, 139–146 (2017).
 19. Wu, S. *et al.* Vapor--solid growth of high optical quality MoS₂ monolayers with near-unity valley polarization. *ACS Nano* **7**, 2768–2772 (2013).
 20. Sakurai, J. J. & Commins, E. D. Modern quantum mechanics, revised edition. (1995).
 21. Griffiths, D. J. & Schroeter, D. F. *Introduction to quantum mechanics.* (Cambridge University Press, 2018).
 22. Briggs, D. Handbook of X-ray Photoelectron Spectroscopy CD Wanger, WM Riggs, LE Davis, JF Moulder and GE Muilenberg Perkin-Elmer Corp., Physical Electronics Division, Eden Prairie, Minnesota, USA, 1979. 190 pp. \$195. *Surf. Interface Anal.* **3**, v--v (1981).
 23. der Heide, P. *X-Ray photoelectron spectroscopy.* (Wiley Online Library, 2011).
 24. Hofmann, S. *Auger-and X-ray photoelectron spectroscopy in materials science: a user-oriented guide.* **49**, (Springer Science & Business Media, 2012).
 25. Agostinelli, E., Battistoni, C., Fiorani, D., Mattogno, G. & Nogues, M. An XPS study of the electronic structure of the Zn_xCd_{1-x}Cr₂ (X= S, Se) spinel system. *J. Phys. Chem. Solids* **50**, 269–272 (1989).
 26. Babot, D. & Chevreton, M. Conductibilité électrique aux basses températures des composés binaires Cr₂X₃ et Cr₃X₄ (X = S, Se ou Te). *J. Solid State Chem.* **8**, 166–174 (1973).
 27. Behrens, M., Kiebach, R., Bensch, W., Häussler, D. & Jäger, W. Synthesis of thin Cr₃Se₄ films from modulated elemental reactants via two amorphous intermediates: a detailed examination of the reaction mechanism. *Inorg. Chem.* **45**, 2704–2712 (2006).
 28. Tang, Q. *et al.* Structure et conductibilité électrique des composés à lacunes ordonnées du système chrome-sélénium. *J. Solid State Chem.* **8**, 2704–2712 (2018).
 29. Carver, J. C., Schweitzer, G. K. & Carlson, T. A. Use of X-Ray photoelectron spectroscopy to study bonding in Cr, Mn, Fe, and Co compounds. *J. Chem. Phys.* **57**, 973–982 (1972).
 30. Charifi, Z., Guendouz, D., Baaziz, H., Soyalp, F. & Hamad, B. Ab-initio investigations of the structural, electronic, magnetic and mechanical properties of CrX (X= As, Sb, Se, and Te) transition metal pnictides and chalcogenides. *Phys. Scr.* **94**, 15701 (2018).
 31. Chen, Z., Higgins, D., Yu, A., Zhang, L. & Zhang, J. A review on non-precious metal electrocatalysts for PEM fuel cells. *Energy Environ. Sci.* **4**, 3167–3192 (2011).

32. Shieh, M. *et al.* Chromium - Manganese Selenide Carbonyl Complexes : Paramagnetic Clusters and Relevance to C d O Activation of Acetone. 8056–8066 (2010). doi:10.1021/ic101118y
33. Corliss, L. M., Elliott, N., Hastings, J. M. & Sass, R. L. Magnetic structure of chromium selenide. *Phys. Rev.* **122**, 1402 (1961).
34. Folmer, J. C. W. & Jellinek, F. The valence of copper in sulphides and selenides: an X-ray photoelectron spectroscopy study. *J. Less Common Met.* **76**, 153–162 (1980).
35. Heine, T. Transition metal chalcogenides: ultrathin inorganic materials with tunable electronic properties. *Acc. Chem. Res.* **48**, 65–72 (2014).
36. Ivanova, V. A., Abdinov, D. S. & Aliev, G. M. On some characteristics of chromium selenides. *Phys. status solidi* **24**, K145--K147 (1967).
37. Kittel, C., McEuen, P. & McEuen, P. *Introduction to solid state physics.* **8**, (Wiley New York, 1976).
38. Lupu, D. & Bucur, R. V. Possible anionic clusters and mixed valence effects in transition metal chalcogenides and oxides. *J. Phys. Chem. Solids* **39**, 285–290 (1978).
39. Lüth, H. & Lèuth, H. *Solid surfaces, interfaces and thin films.* **4**, (Springer, 2001).
40. Meyer, E., Hug, H. J. & Bennewitz, R. *Scanning probe microscopy: the lab on a tip.* (Springer Science & Business Media, 2013).
41. Shenasa, M., Sainkar, S. & Lichtman, D. XPS study of some selected selenium compounds. *J. Electron Spectros. Relat. Phenomena* **40**, 329–337 (1986).
42. Xie, W.-H., Xu, Y.-Q., Liu, B.-G. & Pettifor, D. G. Half-metallic ferromagnetism and structural stability of zincblende phases of the transition-metal chalcogenides. *Phys. Rev. Lett.* **91**, 37204 (2003).
43. Yuan, H., Kong, L., Li, T. & Zhang, Q. A review of transition metal chalcogenide / graphene [32 _ TD \$ IF] nanocomposites for energy storage and conversion. **28**, 2180–2194 (2017).
44. Shivayogimath, A. *et al.* A general approach for the synthesis of two-dimensional binary compounds. *arXiv preprint arXiv:1805.08002* (2018).
45. Tang, Q., Liu, C., Zhang, B. & Jie, W. Synthesis of sub-micro-flakes CrSe₂ on glass and (110) Si substrates by solvothermal method. *Journal of Solid State Chemistry* **262**, 53–57 (2018).
46. der Heide, P. A. W. Multiplet splitting patterns exhibited by the first row transition metal oxides in X-ray photoelectron spectroscopy. *J. Electron Spectros. Relat. Phenomena* **164**, 8–18 (2008).
47. Wang, Q. H., Kalantar-Zadeh, K., Kis, A., Coleman, J. N. & Strano, M. S. Electronics and optoelectronics of two-dimensional transition metal dichalcogenides. *Nature*

nanotechnology **7**, 699 (2012).

48. Wintenberger, M., André, G. & Hammann, J. Composition and temperature dependent magnetic structures of monoclinic chromium selenides Cr_3Se_4 , $x \leq 0.2$. *J. Magn. Mater.* **147**, 167–176 (1995).